Precise Tracking And Initial Segmentation of Abdominal Aortic Aneurysm

Shwu-Huey Yen* Hung-Zhi Wang
Dept. of Computer Science and Information Engineering
Tamkang University
New Taipei City 25137, Taiwan, R. O. C.
*105390@mail.tku.edu.tw

Hsiao-Wei Chang
Dept. of Computer Science and Information Engineering
China University of Science and Technology
Taipei City 11581, Taiwan, R. O. C.

***Abstract*—In this paper we propose a mean-shift based technique for a precise tracking and segmentation of abdominal aortic aneurysm (AAA) from computed tomography (CT) angiography images. The proposed method applies median filter on the gradient of ray-length and linear interpolation for de-noising. The segmentation result can be used for measurement of aortic shape and dimensions. Knowledge of aortic shape and size is very important for selection of appropriate stent graft device for treatment of AAA. Comparing to conventional approaches, our method is very efficient and can save a lot of manual labors.**

Keywords—Aneurysm, Abdominal Abnormal Aneurysm (AAA) ; mean-shift; computed tomography (CT)

I. INTRODUCTION

Aneurysm is an abnormal dilation of the aortic to greater than 1.5 times normal; the diameter of normal aortic vessel is about 1.5 to 2 cm; usually arises in the thoracic aortic or abdominal aortic. Fig.1 shows an aortic figure where A is a normal aortic, B and C show thoracic aortic aneurysm (TAA) and abdominal aortic aneurysm (AAA), respectively. Aneurysm usually represents an underlying weakness in the wall of the aorta at that location. The stretched vessel has a great concern of the rupture risk, which causes severe pain, massive internal hemorrhage, and death if not treated immediately [1]. In general, the aortic aneurysm slowly swells when it starts and grows up much faster when the size of aneurysm becomes larger. Due to rupture risk, physicians must carefully monitor the size and the growth rate of an aortic aneurysm. The monitoring task usually is done by ultrasound or computed tomography (CT). Fig. 2 is a patient's image who has the ruptured abdominal aneurysm. The diameter of abdominal aneurysm is more than 5 cm or the diameter of thoracic aortic aneurysms is more than 6 cm is clinically advised of received surgical treatment. The common treatment is stent graft fitting by surgical operation. The stent is a mesh-like metallic mini tube. It can provide the power of support for vessel wall and reduces the probability of narrowing after angioplasty [2].

The x-ray, ultrasound, CT, magnetic resonance imaging, angiocardiography, and positron emission tomography are common ways to acquire medical images. Among these medical images, CT scanning can accurately demonstrate dilation of the aorta and involvement of major branch vessels proximally and distally. This information helps in determining the appropriate intervention, which may be either surgical or endovascular repair. CT has emerged as the diagnostic imaging standard for the evaluation of AAA, with an accuracy that approaches 100% [3].

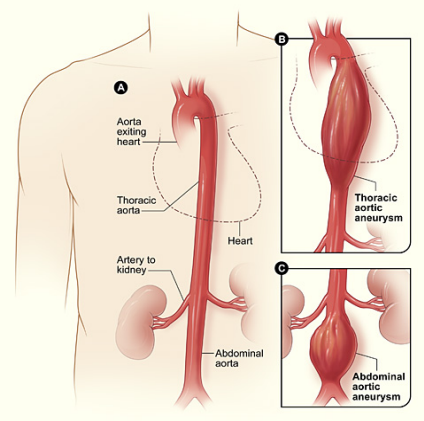

Fig. 1. Aortic image where **A** is a normal aorta, **B** is a thoracic aortic aneurysm (TAA), and **C** shows an abdominal aortic aneurysms (AAA).

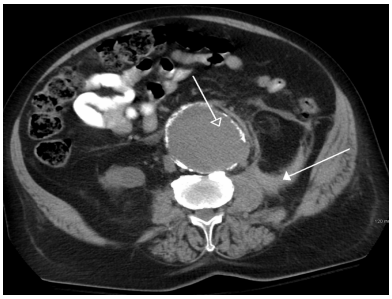

Fig. 2. Ruptured abdominal aneurysm. Hollow arrow points at aortic aneurysms, and solid arrow means that blood flow to abdomen. (by James Heilman, MD [4])

Once a CT slices is obtained, a physician has to locate and measure the size of aortic aneurysm if there is any slice-wise, which is a labor extensive task. While there are many existing image segmentation methods, traditional methods such as Canny, Sobel, Laplace, may not yield satisfactory results. As observed in Fig. 3, the ideal segmentation would be along the contour of the lumen, i.e., the epithelial tissue. But the surrounding organ tissues are very similar to the epithelial one's not to mention that the possible calcifications and stents appear in the lumen.

To solve this problem, several researches have devoted to the issue of AAA image segmentation. These methods can be categorized into automatic and semi-automatic segmentation. The former means that users need not input any parameters and the system will locate the AAA. In [5-6], they used fuzzy C-mean and generated a binary image indicating lumen as well as possible AAA. However, users have to align both the CT slice and its binary result to obtain more detail information of the AAA position. The latter means that users have to set up some variable and/or give initial definitions before the system to locate the region of interest (ROI). Among these semi-automatic methods, they can further be classified as machine learning and non-machine learning.

Marko [7] proposed an AAA segmentation of non-machine learning in 2002. It requires users to provide the AAA deformable model of the patient. They used two thresholds to filter noises and distance gradient to obtain the segmentation, finally, refine the result by the defined model. However, every patient has his/her own complication and the default parameters may not suitable for every condition.

In 1995, Cootes [8] proposed a machine learning method-Active Shape Model (ASM) to segment AAA. Based on ASM, Marleen [9] proposed an interactive segmentation of AAA in CTA images in 2003. Users need to mark the region of AAA on first CT. Then the system will segment the next slice according to the previous one. Users can adjust the contour if necessary. The major commercial software is implemented likewise. While [8] always exploits the first segmented slice to obtain the segmentation of the rest slices, [9] utilizes the previous slice of current one instead. In 2005, inspired by [11], Silvia [10] used minimum cost path to track aorta in CT slices. The method integrates the ASM of [9] and K-NN of [12] to tackle the blurring contour problem. In these ASM model based methods, they need to define an initial model previously. In this paper, we propose a semi-automatic method which only needs simple operations to complete the initial segmentation of the AAA.

II. Proposed Method

The CT scanner uses a set of software algorithms to determine the amount of x-radiation absorbed by every element in a plane of tissue. Each of these elements is represented by a pixel on the slice display, and the density (amount of x-radiation absorbed) is measured in Hounsfield units (HU). To view a CT scan slice, users choose the window width (W), which describes the range of HU displayed. Next, users choose the window level (L) which is the Hounsfield number in the center of the window width. In our algorithm, we use HU values for calculation. Fig. 4 gives a flowchart of the proposed method and each step is described in the following.

A. Set Up Starting and Ending Slices

Similar to Wörz et al. [13], users need to indicate the starting and ending slices for the proposed method. To fully access the information, we label a small box inside the lumen on the starting slice. From the indicated box, not only the starting slice is determined but the mean $M_{L,0}$ and the standard deviation $\sigma_{L,0}$ of lumen are evaluated. As shown in Fig. 5, the user simply labels a small box inside the lumen (shown in red) and the system obtains the initial lumen centre and a suitable threshold for image binarization explained below.

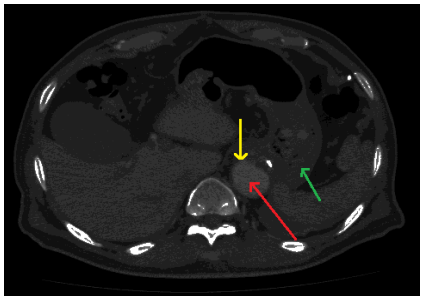

Fig. 3. AAA and the surrounding organs. Red arrow points at the area of lumen, yellow arrow is the epithelial tissue, and green arrow points the surrounding organ tissue.

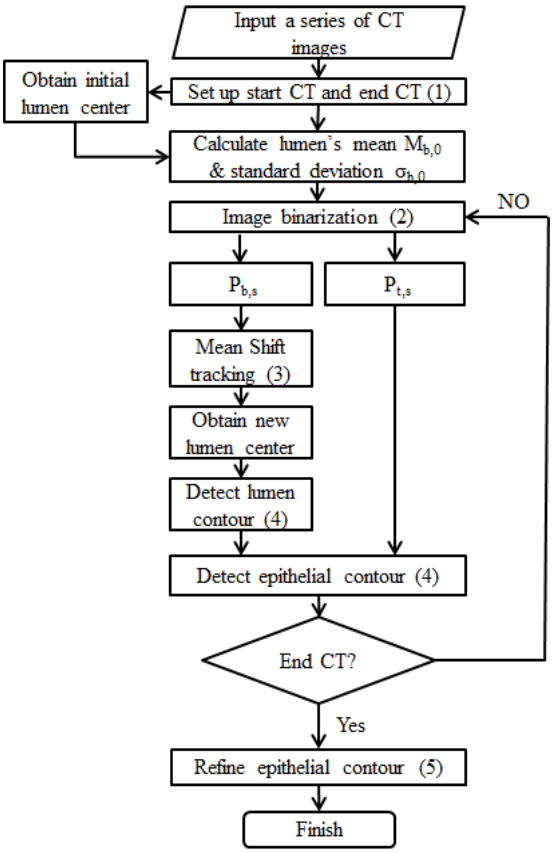

Fig. 4. The flowchart of the proposed method.

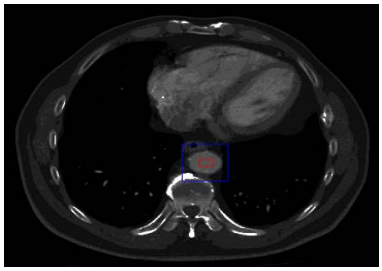

Fig. 5. Initial setting. User labels a region (the red box) inside the lumen. Centered at the red box, the blue box is generated automatically and it is used for abdominal aorta tracking.

B. *Image binarization*

Two binarized images are produced for ROIs of lumen and epithelia which are used for contour detection later. Equation (1) is to get lumen's binarized image. The result is in Fig. 6(a), and 6(b) is a result after closing operation in Morphological Image Processing [14].

$$P_{L,s}(x,y)=\begin{cases}1 & |H(x,y)-M_{L,s}|\le \alpha\cdot\sigma_{L,s}\\ 0 & otherwise,\end{cases} \quad (1)$$

where $H(x,y)$ represents the input HU value at (x, y) position, $M_{L,s}$ and $\sigma_{L,s}$ is the mean and standard deviation of HU values of the lumen in slice s. In our experiment, α is chosen to be three. We use equation (2) to get epithelia's binarized image.

$$P_{E,s}(x,y)=\begin{cases}1 & 0\le H(x,y)\le 50\\ 0 & otherwise.\end{cases} \quad (2)$$

Since that stent would affect the system to detect the epithelia's contour, we use (3) to get stent's binarized image.

$$P_{Stent,s}(x,y)=\begin{cases}1 & H(x,y)\ge 350\\ 0 & otherwise.\end{cases} \quad (3)$$

The HU range for a stent is 700–1000 as suggested by the physicians. But, in our observation, quite a few stent images have HU values much less than the suggested values. That is due to the possible tissue coverage on the stents after a period of time when the stent graft fitting surgical operation has been executed. Therefore, we choose 350 as the threshold in (3).

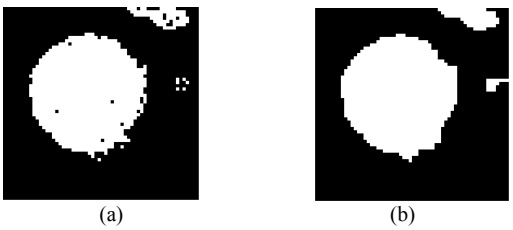

(a) (b)

Fig. 6. Binarization. (a) binarized lumen image, (b) the hole-filling image of (a) by closing operation.

In order to reduce the influence of stent, we use (4) to obtain an appropriate epithelia's binarized image. Fig. 7 shows an example. The epithelial region in (a) is the area between two green circles (the inner circle is the lumen), (b) is binarized result for epithelia which also includes the lumen area. Since the contour of epithelia is our concern, the lumen area will not cause any problem. However, the white spot inside (pointed by the green arrow) and two overflow areas (indicated in red) may cause problems. We will explain how to overcome these problems in Section *D*.

$$\{P_{E,s}(x,y)\}\leftarrow\{P_{E,s}(x,y)\}\cup\{P_{Stent,s}(x,y)\}. \quad (4)$$

C. *Mean shift tracking*

From the lumen center and lumen's binarized image of the previous slice, we use weighted kernel Mean shift algorithm [15] to track abdominal aorta. Equation (5) is the Gaussian kernel which gives more weights for points near the center position (lumen center) and equation (6) is to evaluate the new center c = (X_{center}, Y_{center}) for the current slice. More details are referring to [15]. Fig. 8 illustrates some tracking results.

$$G(x,y)=\frac{1}{2\pi\sigma^2}\exp\left(-\frac{1}{2}\cdot\frac{(x-Height/2)^2+(y-Width/2)^2}{\sigma^2}\right). \quad (5)$$

$$X_{center}=M_{10}/M_{00} \quad \text{and} \quad Y_{center}=M_{01}/M_{00}, \quad (6)$$

where

$$M_{00}=\sum_{(x,y)\in Box}G(x,y),$$

$$M_{10}=\sum_{(x,y)\in Box}x\cdot G(x,y),$$

$$M_{01}=\sum_{(x,y)\in Box}y\cdot G(x,y).$$

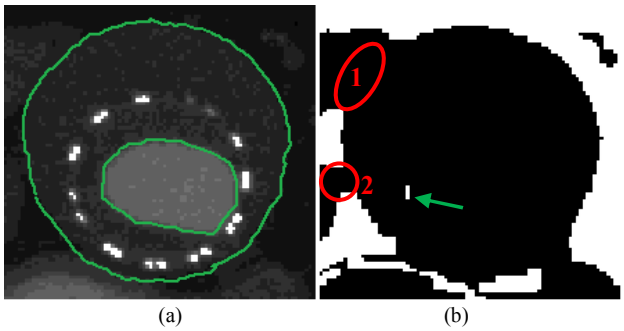

(a) (b)

Fig. 7. (a) the ideal epithelial region is between two green circles, (b) the result of our binarized image of epithelia; the indicated areas may cause error in contour detection.

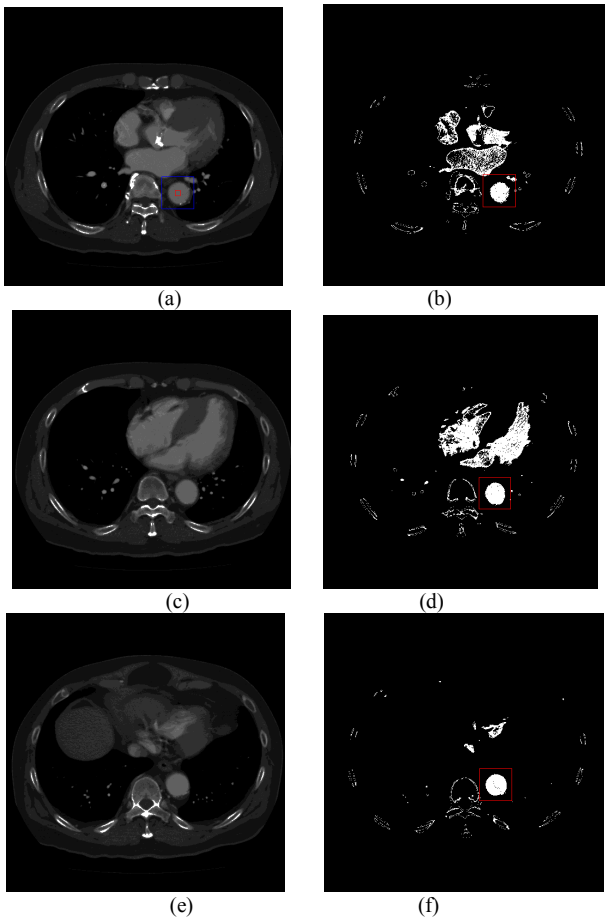

Fig. 8. (a), (c), (e) are the 1st, 9th, 17th slices. Red box on (b), (d), (f) are the mean-shift tracking results of abdominal aorta in (a), (c), (e), respectively.

D. *Lumen and epithelial contours detection*

We first define the ROIs for lumen and epithelial. The binary image obtained from (1) and the mean shift algorithm is used as the lumen ROI, such as in Fig. 6(b), and 8 (b), (d), (f). The binary image obtained from (4) is used as the epithelial ROI, such as in Fig. 7(b).

Inspired by [16], we use ray-detection method as in Fig. 9 where c= (X_{center}, Y_{center}) is from (6). Starting from c, equal angle rays are casted and a ray stops when the immediate next point falls outside the ROI. A median filter is applied next. Initial contours are obtained by connecting the end points of the casting rays. In Fig. 10, a ray detection result is shown where red circle is the lumen contour and green circle is the epithelial contour. Unlike the lumen contour, it can be seen that epithelial contour is not as stable. The length of rays may increase (if there is an overflow area in the ROI, e.g., the red circles in Fig. 7 (b)) and/or decrease (if there is a noise, e.g., stent as in the green arrow in Fig. 7(b)) rapidly which cause error contour. Based on the assumption that the contour is approximate oval shaped, the derivative in the radius (i.e., ray length) of neighboring rays should be small. Therefore, the first-order derivative of radius, as in (7), can be used to detect abnormal increasing or decreasing in ray length.

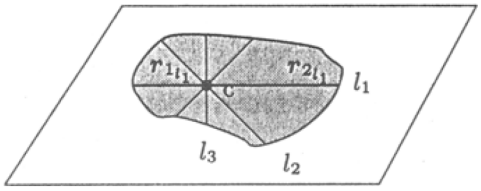

Fig. 9. Ray-detection illustration [16]

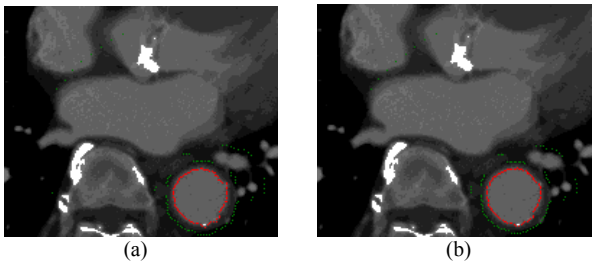

Fig. 10. Ray detection. (a) original result, and (b) after median filter applied where yellow arrows pointing at places to show the before-and-after filtering effect.

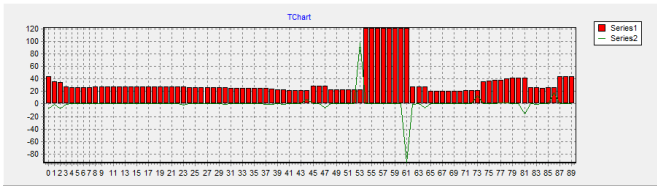

Fig. 11. Red represents the radius of ray-detection (of epithelial) in Fig.10 (b) for $\Delta\theta = 4^{o}$, and green represents first-order derivative of radius.

$$R'(s,\theta) = R(s,\theta+\Delta\theta) - R(s,\theta), \tag{7}$$

where $R(s, \theta)$ represents the radius on the angle θ of the slice s, and $\Delta\theta = 360^{o}/n$ with n = 90 used here. In Fig. 11, horizontal axis shows zeroth ray to 89th ray of Fig. 10(b), the height of the red bin shows the radius, and the green curve indicates the derivative result from (7). We sort the absolute values of all derivatives of (7) and discard the first and last 10% of the data to reduce outliers. Then, the typical magnitude of derivatives is taken as the mean value of the rest of data. Using this value as the threshold (Th) in (8), we classify rays that are rapidly changed. A matrix T of size $1 \times n$ is used to store the markers for rays. As in (8), the marker f_1 represents the ray that the radius increases rapidly, the marker f_2 represents the ray where the radius decreases rapidly, and the marker 0 for the rest of cases.

$$T[r] = \begin{cases} f_1 & |R'(s, r\cdot\Delta\theta)| > Th \;\&\; R'(s, r\cdot\Delta\theta) > 0 \\ f_2 & |R'(s, r\cdot\Delta\theta)| > Th \;\&\; R'(s, r\cdot\Delta\theta) < 0 \\ 0 & otherwise, \end{cases} \tag{8}$$

where r is the ray index, r = 0, 1, ..., (n-1). Starting from the ray with the shortest radius clockwise, the marker is checked one by one. Once a pair of f_1 (e.g., located at ray i) and f_2 (e.g., located at ray j) is found, rays falling between them will be linear interpolated. Equation (9) explains the linear interpolation using $R(s, i)$ and $R(s, j+1)$ where K is the number of rays to be interpolated.

$$R(s,(i+k) \bmod n) = R(s,i) + k \cdot \delta, \quad \kappa = 1, 2, ..., K, \qquad (9)$$

where

$$K = \begin{cases} j+1-i & j > i \\ (n+j+1)-i & otherwise, \end{cases}$$

$$\delta = (R(s,(j+1)) - R(s,i))/K.$$

When a pair of f_1 and f_2 is found, we need to further check whether the range between them is greater than 120°. Since when there is an aneurysm, radii may increase (as in Fig. 14 c-3) but radii stay large for a wide range. Figure 12 is the result after (9) is executed. Comparing to Fig. 10(b), error epithelia contour has been fixed nicely.

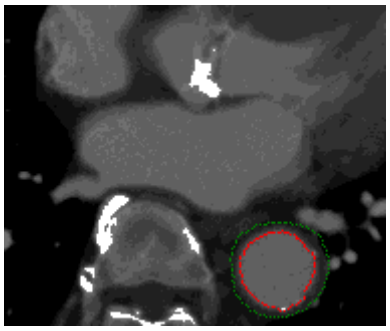

Fig. 12. Result of Fig. 10(b) after linear interpolation adjustment.

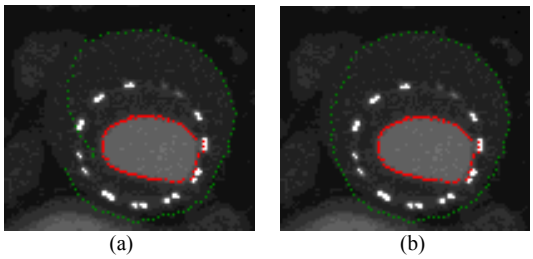

(a) (b)

Fig. 13. Epithelia contour detection of the image in Fig. 7. (a) is the result after linear interpolation, overflows are fixed but the error caused by stent noise remains; (b) refined result after temporal median filter on 5 consecutive slices.

E. Refine Epithelial Contour

As mentioned in Fig. 7(b), the indicated areas may cause errors in contour detection. Once the initial epithelial contour is obtained, linear interpolation is executed if there is any pair of f_1 and f_2. Fig. 13(a) shows the result after linear interpolation. of (9) is executed. As observed, the bottom and the top of the red circle 1 (as indicated in Fig. 7(b)) constitute a pair of f_1 and f_2 and it is fixed nicely. However, linear interpolation may fail too. The ray positioned at the green arrow is the shortest ray (f_1) which erroneously stops because of the noise; the ray near the top of the red circle 2 is f_2 since the ray length becomes short suddenly. After the implementation of linear interpolation, neither it produces the correct ray length on f_1 position nor the ray lengths between f_1 and f_2. A temporal median filter is applied to solve this problem. On each ray of the same angle among consecutive slices, we use the median filter on the radius on five consecutive slices s, s±1, s±2, i.e., the median filter on the temporal axis. Fig. 13(b) shows the refined result.

III. Experimental Results

To validate the method, we use a normal example and eight abdominal aortic aneurysm examples. The range of age in nine patients is 60-85. Due to limited space, we present the result of one normal and three AAA examples in Fig. 14. The complete nine experimental results may be seen on [17]. In Fig.14, row (a) is the normal case, and next three rows (b)–(d) are three AAA cases; column (1) shows the starting slices, column (2) shows the slices near renal artery (branch of abdominal aorta), and column (3) shows the end slices. The proposed method is effective as observed in Fig. 14. In particular, in (a-3), our method is robust to the vascular calcification. While most of segmented results are accurate, sometimes the detected epithelia contour is wider than it is as in (c-2 & d-2). This is due to the process of reducing the influence from the stent, as well as too many similar tissues.

IV. Conclusion

We proposed a method which only requires a user to label a small box in the starting slice and indicates where the end slice is. Our method can automatically use the initial information to track abdominal aortic aneurysm using weighted mean shift algorithm. Linear interpolation in spatial and median filter in temporal are used to detect contours. A satisfactory result is obtained using our method. The result can be a pre-process of AAA localization if there is any. In order to be clinical useful, we will test our system by more examples in the future. Finally, our method can combine clustering algorithm to track the common iliac artery.

Acknowledgment

The authors would like to express their gratitude to the doctors of Taipei Veterans General Hospital who provided CT slices as well as professional consultations.

References

[1] "Aortic aneurysm," [Online]. Available: http://en.wikipedia.org/wiki/Aortic_aneurysm

[2] C.-C. Shih, MD, PhD., "New era of mini-invasive treatment of aortic aneurysm," *Clinical Medicine,* vol. 10, pp. 271-282, 2007.

[3] M. G. Radvany and V. Seguritan, "Abdominal aortic aneurysm imaging," Medscape Reference, 11 2012. [Online]. Available: http://emedicine.medscape.com/article/416266-overview.

[4] J. Heilman, MD, "A ruptured AAA as seen on CT," 2 June 2011. [Online]. Available: http://commons.wikimedia.org/wiki/File:RupturedAAA.png

[5] T. D. Pham and J. Golledge, "Geo-statistically constrained fuzzy Ssegmentation of abdominal aortic aneurysm CT images," *IEEE International Conference on Fuzzy Systems, 2008. FUZZ-IEEE 2008. (IEEE World Congress on Computational Intelligence).,* pp. 1446 - 1451, June 2008.

[6] E. M, Majd, U. U. Sheikh, and S.A.R Abu-Bakar, "Automatic segmentation of abdominal aortic aneurysm in computed tomography images using spatial fuzzy C-means," *Signal-Image Technology and Internet-Based Systems (SITIS), 2010 Sixth International Conference on,* pp. 170 - 175, 2010.

[7] M. Subasic, S. Loncaric, and E. Sorantin, "3D image analysis of abdominal aortic aneurysm," *SPIE Medical Imaging,* p. 388, 2001.

[8] T. F. Cootes, C. J. Taylor, D. H. Cooper, and J. Graham, "Active shape models-their training and application," *Computer Vision and Image Understanding,* vol. 61, no. 1, pp. 38-59, 1995

[9] M. N de Bruijne, B. van Ginneken, M. A. Viergever, and W. J. Niessen, "Interactive segmentation of abdominal aortic aneurysms in CTA images," *Medical Image Analysis,* vol. 8, no. 2, pp. 127-138, 2004.

[10] S. D. Olabarriaga, J.-M. Rouet, M. Fradkin, M. Breeuwer, and W. J. Niessen, "Segmentation of thrombus in abdominal aortic aneurysms from CTA with nonparametric statistical grey level appearance modeling," *Medical Imaging, IEEE Transactions,* vol. 24, no. 4, pp. 477-485, 2005.

[11] O. Wink, W. J. Niessen, and M. A. Viergever, "Minimum Cost Path Determination Using a Simple Heuristic Function," *Pattern Recognition, 2000. Proceedings. 15th International Conference,* vol. 3, pp. 988-1001, 2000

[12] S. Arya, D. M. Mount, N. S. Netanyahu, R. Silverman, and A. Y. Wu, "An optimal algorithm for approximate nearest neighbor searching fixed dimensions," *Journal of the ACM,* vol. 45, no. 6, pp. 891-923, 1998.

[13] S. Wörz, H. von Tengg-Kobligk, V. Henninger, F. Rengier, H. Schumacher, and D. Böckler, H.-U. Kauczor, and K. Rohr, "3-D quantification of the aortic arch morphology in 3-D CTA data for endovascular aortic repair," *IEEE Transactions on Biomedical Engineering,* vol. 57, pp. 2359-2368, 2010.

[14] E. R. Dougherty, An introduction to morphological image processing, SPIE Optical Engineering Press, 1992.

[15] Y. Cheng, "Mean shift, mode seeking, and clustering," *IEEE Transactions on Pattern Analysis and Machine Intelligence,* vol. 17, pp. 790-799, 1995

[16] O. Wink, W. J. Niessen, and M. A. Viergever, "Fast quantification of abdominal aortic aneurysms from CTA volumes," *Medical Image Computing and Computer-Assisted Intervention — MICCAI' 98 Lecture Notes in Computer Science,* vol. 1496, pp. 138-145, 1998

[17] [Online]. Available: http://http://youtu.be/ihD-byMREWI; http://youtu.be/XREV74msJZ0; http://youtu.be/ruQWZrpXSAs; http://youtu.be/VRaJl9VJ9CQ; http://youtu.be/ODhLCypaWI8; http://youtu.be/g-JOtCfGXhQ; http://youtu.be/rW-54-SnSVU; http://youtu.be/VixV6SSRdfs; http://youtu.be/lKkiG5TMdv4

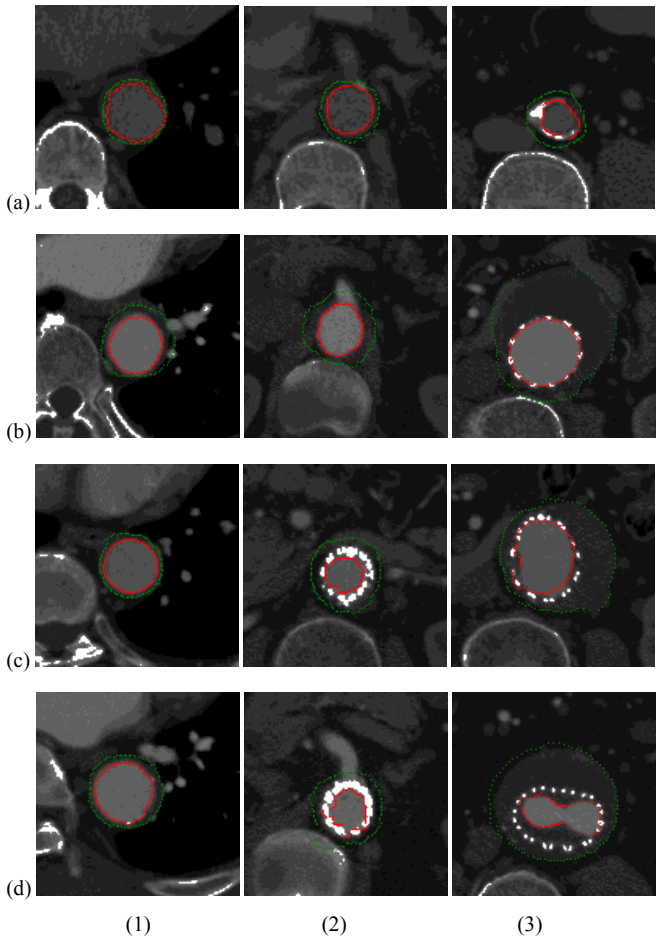

Fig. 14. row: (a) normal example, (b)(c)(d) AAA examples; column: (1) start slice, (2) branch of abdominal aorta (renal artery), (3) end slice.